Dynamic sound scattering: Field fluctuation spectroscopy with singly scattered ultrasound in the near and far fields

M. L. Cowan and J. H. Page[a)]
Department of Physics and Astronomy, University of Manitoba, Winnipeg, Manitoba R3T 2N2, Canada

T. Norisuye
Department of Macromolecular Science and Engineering, Graduate School of Science and Technology, Kyoto Institute of Technology, Kyoto 606-8585, Japan

D. A. Weitz
Department of Physics and School of Engineering and Applied Sciences, Harvard University, Cambridge, Massachusetts 02138, USA

(Received 28 March 2016; revised 16 August 2016; accepted 22 August 2016; published online 23 September 2016)

Dynamic sound scattering (DSS) is a powerful acoustic technique for investigating the motion of particles or other inclusions inside an evolving medium. In DSS, this dynamic information is obtained by measuring the field autocorrelation function of the temporal fluctuations of singly scattered acoustic waves. The technique was initially introduced 15 years ago, but its technical aspects were not adequately discussed then. This paper addresses the need for a more complete account of the method by describing in detail two different implementations of this sound scattering technique, one of which is specifically adapted to a common experimental situation in ultrasonics. The technique is illustrated by the application of DSS to measure the mean square velocity fluctuations of particles in fluidized suspensions, as well as the dynamic velocity correlation length. By explaining the experimental and analytical methods involved in realizing the DSS technique in practice, the use of DSS will be facilitated for future studies of particulate suspension dynamics and particle properties over a wide range of particle sizes and concentrations, from millimeters down to nanometers, where the use of optical techniques is often limited by the opacity of the medium.
 [http://dx.doi.org/10.1121/1.4962556]

[MFH] Pages: 1992–2001

I. INTRODUCTION

Ultrasonic waves can be used as a powerful probe of the properties and structure of materials. Ultrasonic velocity and attenuation measurements have been used for decades to characterize the mechanical properties of materials, as well as to learn about their electronic and magnetic excitations. Ultrasonic waves have also been used extensively for nondestructive testing, with common examples ranging from the detection of cracks in airplane wings to the imaging of fetuses. Using Doppler ultrasound techniques,[1] in which the scattering particles move together collectively throughout the scattering volume probed by the ultrasonic beam, the flow velocity of fluids can be measured. However, there are many important cases where the motion of the scattering particles is more complex, requiring new experimental approaches and methods of analysis to extract meaningful information from the scattered ultrasonic signals. To address this limitation, we have developed two powerful ultrasonic correlation spectroscopies, called dynamic sound scattering (DSS) and diffusing acoustic wave spectroscopy (DAWS),[2–4] which exploit, respectively, the dynamic information present in the speckles caused by singly and multiply scattered ultrasound. Speckles occur whenever there are many scatterers in the volume probed in any given instant by the ultrasonic waves; they arise from interference between waves that have traveled different scattering paths through the sample and cause the measured signals to fluctuate with position throughout the detection or image plane. In static imaging applications, speckles have often been regarded as a nuisance since they degrade the quality of the image, and much effort has been expended in trying to minimize this detrimental effect, especially when multiple scattering is involved, through complicated filtering techniques.[5–7] However, speckles also contain considerable information about the dynamics of a moving medium, as was initially demonstrated using DSS and DAWS to investigate the particle velocity fluctuations in fluidized suspensions.[2] In a more recent example, particle motion with different physical origins, such as Brownian motion and sedimentation, has been simultaneously observed using DSS.[8]

These examples show that DSS is emerging as a powerful technique for investigating the complex dynamics of particulate suspensions. Besides thermal fluctuations typically observed in nano-particle suspensions, hydrodynamic interactions dominate the dynamics of micron-sized (and larger) particles. Because of the strong scattering and serious attenuation of light for particles in this size range, such dynamics become more difficult to observe by conventional optical

[a)]Electronic mail: John.Page@UManitoba.ca

techniques, such as dynamic light scattering (DLS). More recently, alternative DLS approaches combining an interferometer to probe particle motion at the shallow surface of a suspension have been proposed to overcome this problem, although the applications are more or less limited to submicron particles at moderate concentrations.[9,10] For this reason, the DSS techniques provide a complementary tool to investigate dynamics of particles, especially for larger particle sizes at higher concentrations, and they have been utilized to investigate the average particle velocities and velocity fluctuations in fluidized[2] and sedimenting[11,12] suspensions. Another advantage of using pulsed ultrasound is its ability to measure phase,[13] which contains the particles' spatio-temporal information. The single-scattering acoustic techniques are utilized to evaluate instantaneous particle velocities by capitalizing on these advantages,[14] as described below.

Among the versatile fields of research interests in particulate suspensions, hydrodynamic interactions have especially attracted the attention of researchers in complex fluid dynamics.[15–17] For example, while the sedimenting particles' velocity field may seem to be apparently uniform in the flow direction, its deviation from the average reveals that there exists a unique dynamic structure accompanying cooperative domains ("blobs"), and the size of each domain is surprisingly large (often on the order of millimeters) compared with the individual particle size (often only a few microns). Since the phase techniques allow one to extract the instantaneous velocity of settling particles,[14] the sedimentation velocity field can be visualized without scanning the sample.[18] The major cause of velocity fluctuations is now understood to be the number fluctuations of particles in a blob containing the collection of particles having the same velocity due to long-ranged hydrodynamic interactions.[16,19] Furthermore, anomalous velocity fluctuations in charged systems have also been reported recently.

Quite apart from the potential benefits of these sound scattering techniques, the technical aspects have not been adequately addressed yet. Since previous papers on DSS have focused mostly on the information about particle dynamics that has been obtained using this technique, a comprehensive analysis of the experimental methods and theory was outside the scope of these articles, and only an overview of the technical aspects was presented. In addition, there has been no discussion of performing DSS measurements in the near field. Therefore, the purpose of this paper is to describe in detail how the methods of correlation spectroscopy, initially developed in the context of light scattering experiments, can be extended to determine new types of dynamic information from the temporal fluctuations of the ultrasonic speckles. Since the acoustic techniques directly measure the fluctuations of the scattered wave field, rather than the intensity that is probed in the optical techniques, DSS is an example of field fluctuation spectroscopy.

Complex motion of the scatterers causes large temporal fluctuations in the scattered field amplitude at a single speckle, leading to the decay of the temporal field autocorrelation function. For singly scattered ultrasound, the temporal field autocorrelation function can be related to the dynamics by adapting the detailed theoretical formalism first worked out for light.[20] We have developed two different experimental implementations to realize our DSS technique, one of them being especially novel and easier to set up experimentally for acoustic waves. The first follows the traditional approach used in light scattering experiments; there is an incident plane wave, and a detector is placed in the far field to measure the sound scattered at a particular scattering angle. The second implementation of single scattering spectroscopy takes advantage of the fact that ultrasonic measurements are often best performed in the near field. This approach is made possible by performing these experiments with short pulses, rather than with continuous waves as in most laser light scattering experiments. As an example, we show how DSS can be used to measure the root mean square velocity fluctuations and the velocity correlation time of millimeter-sized particles that are suspended in a liquid by fluidizing the suspension.

II. THEORY

In DSS, the experiments measure the temporal fluctuations of the scattered pressure field $\psi(t)$ due to the superposition of a large number of single scattered contributions. As described in Sec. III, the experiments capitalize on the advantages of pulsed techniques, and measure the temporal evolution the scattered field as the scatterers move at observation times t determined by multiples of the pulse repetition rate. This evolution time t is much greater than the propagation time of the ultrasonic pulse in the medium, with the field being sampled at a fixed propagation time after the pulse is incident on the sample. The motion of the scattering particles is then determined over the evolution time interval $\tau = \Delta t$ directly from the field autocorrelation function

$$g_1(\tau) = \frac{\int \psi(t)\psi^*(t+\tau)dt}{\int |\psi(t)|^2 dt}. \tag{1}$$

The field can be written as a sum over contributions from all of the different paths through the sample (or equivalently as a sum over all of the scatterers in the scattering volume)

$$\psi(t) = \sum_p \psi_p(t) = A \sum_p \exp\left[i\phi_p(t)\right], \tag{2}$$

where A is the single scattering amplitude and ϕ_p is the phase of the scattering path p. This leads to

$$g_1(\tau) = \frac{\left\langle \sum_{p,p'} \exp\left[i\{\phi_p(t) - \phi_{p'}(t+\tau)\}\right] \right\rangle_t}{\left\langle \sum_{p,p'} \exp\left[i\{\phi_p(t) - \phi_{p'}(t)\}\right] \right\rangle_t}. \tag{3}$$

Here $\langle \cdots \rangle_t$ denotes an average over t. For scatterers that are randomly distributed in space, only the terms with $p = p'$ will survive the time average in the numerator and denominator.[21] To show this explicitly, we write

$$\phi_p(t) = \vec{q} \cdot \vec{r}_p(t),$$
$$\phi_{p'}(t+\tau) = \vec{q}[\vec{r}_{p'}(t) + \vec{r}_{p'}(t+\tau) - \vec{r}_{p'}(t)]$$
$$= \vec{q}[\vec{r}_{p'}(t) + \Delta\vec{r}_{p'}(\tau)], \quad (4)$$

where $\vec{q} = \vec{k}' - \vec{k}$ is the scattering wave vector [the difference between the scattered ($\vec{k}'$) and incident ($\vec{k}$) wave vectors], $\vec{r}_p$ is the position of the pth particle, and $\Delta\vec{r}_p(\tau)$ is its change in position from time t to time $t+\tau$. Then the numerator in Eq. (3) becomes

$$\left\langle \sum_{p,p'} \exp[i\vec{q}\{\vec{r}_p(t) - \vec{r}_{p'}(t)\}] \exp[-i\vec{q} \cdot \Delta\vec{r}_{p'}(\tau)] \right\rangle_t. \quad (5)$$

For random particle positions, and assuming that the average motion of the particles is independent of position, the first exponential will fluctuate and cause the average to be zero, unless the term in curly brackets is identically equal to zero for all times t. This will only happen for all times if $p = p'$. A similar argument holds for the denominator as well.

Returning to Eq. (3), we can now write it as

$$g_1(t) = \frac{\left\langle \sum_p \exp[-i\Delta\phi_p(\tau)] \right\rangle}{N} = \frac{\sum_p \left\langle \exp[-i\Delta\phi_p(\tau)] \right\rangle}{N}$$
$$= \langle \exp[-i\Delta\phi(\tau)] \rangle, \quad (6)$$

where $\Delta\phi(\tau)$ is the change in the phase of a single path over a time τ, due to the motion of the scatterer. Since the phase fluctuations $\Delta\phi(\tau)$ are expected to be randomly distributed about an average value $\langle\Delta\phi(\tau)\rangle$ equal to zero, these deviations should follow a Gaussian distribution with zero mean due to the central limit theorem. Hence, the average value of $\exp[-i\Delta\phi(\tau)]$ in Eq. (6) becomes

$$g_1(\tau) \sim \exp\left[-\frac{1}{2}\langle\Delta\phi^2(\tau)\rangle\right] \quad (7)$$

to an excellent approximation. This result can also be obtained by expanding the argument of the exponential in Eq. (6) in a Taylor series:

$$g_1(\tau) = 1 - i\langle\Delta\phi\rangle - \frac{1}{2!}\langle\Delta\phi^2\rangle + \cdots$$
$$= 1 - \frac{1}{2}\langle\Delta\phi^2\rangle + \cdots \sim \exp\left[-\frac{1}{2}\langle\Delta\phi^2(\tau)\rangle\right].$$

As indicated in Fig. 1, the phase change of a path over the time interval τ can be written in terms of the scattering wave vector and the displacement of the scattering particle,

$$\Delta\phi_p = [\vec{k}' - \vec{k}][\vec{r}(t+\tau) - \vec{r}(t)] = \vec{q} \cdot \Delta\vec{r}(\tau). \quad (8)$$

Combining this with Eq. (7) leads to

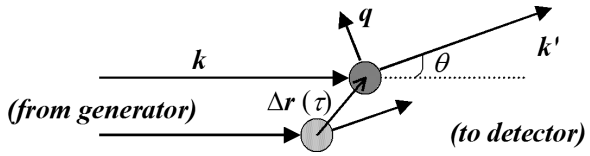

FIG. 1. Single scattering from a moving particle.

$$g_1(\tau) = \exp\left[-\frac{1}{2}\langle[\vec{q} \cdot \Delta\vec{r}(\tau)]^2\rangle\right]$$
$$= \exp\left[-\frac{1}{2}q^2\langle\Delta r_{\vec{q}}^2(\tau)\rangle\right], \quad (9)$$

where $\Delta r_{\vec{q}}$ is the displacement in the direction of the scattering wave vector. Equation (9) shows explicitly that DSS is only sensitive to the mean square displacement in the direction of $\vec{q}$, which is determined by the scattering geometry.

III. EXPERIMENT

Both the near and far field experimental configurations used pulsed ultrasonic techniques to capitalize on their many advantages for DSS measurements, as described in detail in the following paragraphs. The scattered field was measured at the same propagation time in each transmitted pulse using a boxcar integrator, which allowed the waveform voltage (proportional to the acoustic field) to be measured over a narrow time window (set to approximately 30 ns in our measurements, which is very much less than the 4 μs period of the waves) centered at a particular propagation time near the middle of each pulse. The boxcar integrator outputs this voltage until the next trigger is received, whereupon it samples the input again and resets the output, allowing the field fluctuations due to the motion of the scatterers to be measured at a rate determined by the pulse repetition frequency. Alternatively, if a sufficiently rapid digitizing system is available (e.g., an oscilloscope card/computer combination), the entire scattered pulse can be digitized and stored, enabling post-processing of the data to determine the evolution of the field at a particular propagation or sampling time. Figure 2(a) shows an example of the evolution time dependence of the field fluctuations that were measured as the scatterers move. The field autocorrelation function [Eq. (1)] was then calculated from the field fluctuation data by taking fast Fourier transforms and using the correlation theorem.[22] Figures 2(b) and 2(c) show the autocorrelation function for the data in Fig. 2(a). Using the theory developed in Sec. II, the mean square displacement of the scatterers can be found from the field autocorrelation function if the scattering wave vector $\vec{q}$ is known.

In the far field configuration, the direction of $\vec{q}$ can be chosen by changing the positions of the generating and receiving transducers, and thus the different spatial components of the mean square displacements of the particles can be measured independently. This is illustrated in Fig. 3, where the scattering geometry used to isolate each component of $\langle\Delta r_{\vec{q}}^2(\tau)\rangle$ is shown. By choosing θ_{water} such that the angle in the sample medium is 45°, the scattering angle for the horizontal and vertical setups is 90°, and $\vec{q}$ lies along the x- and y-axis, respectively. The reflection geometry uses the

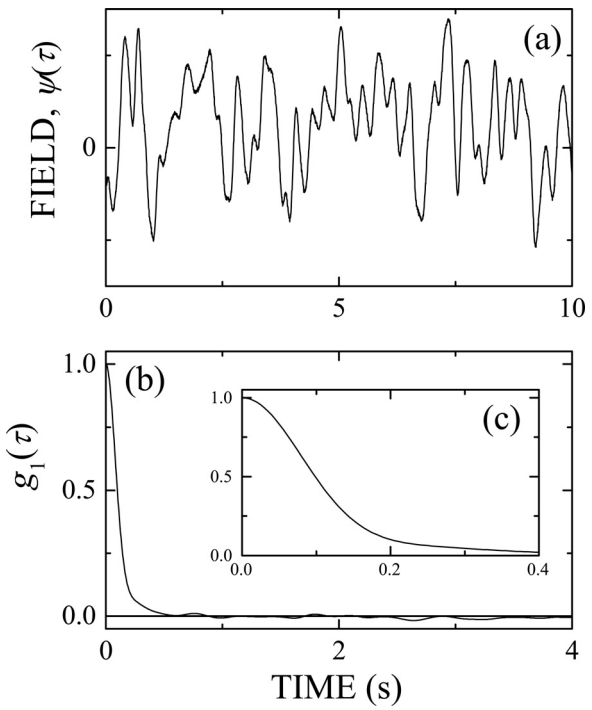

FIG. 2. (a) Measured field fluctuations. (b) The corresponding field autocorrelation function. (c) The field autocorrelation function at early times.

same transducer to generate and detect ultrasound, giving a scattering angle of 180°, and a $\vec{q}$ that lies on the z-axis.

The experiment was performed in a large water tank because of the large path lengths that are needed. The transducers used had flat disk-shaped elements, with a central frequency of 250 kHz and a 1.5 in. diameter. This low frequency was selected to ensure that single scattering was dominant, even in our thickest samples, since the scattering mean free path always was much larger than the sample thickness for the millimeter size solid particles used in these experiments.[23] The pulses used were 20 μs long with a square envelope, giving a reasonable balance between time and frequency widths. As a result, the pulses were sufficiently short to help restrict the range of scattering angles that contribute to the detected signals, as explained in the next paragraph, while the frequency bandwidth (~5%) was sufficiently narrow that dispersive propagation effects did not complicate the analysis. The field was sampled at one particular time in the middle of the spread of arrival times for the scattered waves.

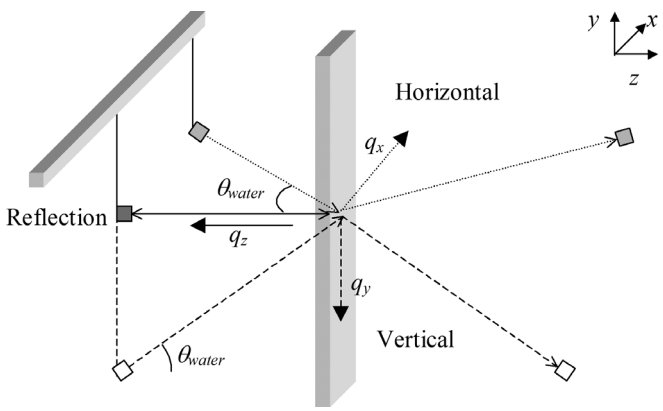

FIG. 3. Far field single scattering geometry. The solid lines show the transducer configuration used to measure the time-dependent mean square displacement along z, $\langle \Delta r_z^2(\tau)\rangle_z$, the dashed lines show the vertical geometry used to measure $\langle \Delta r_y^2(\tau)\rangle_y$, and the dotted lines show the geometry used to measure $\langle \Delta r_x^2(\tau)\rangle_x$. For millimeter sized particles, the mean square displacements are proportional to τ^2 at early times, allowing all three components of the root mean velocity, V_{rms}, to be measured.

There is a range of possible scattering angles that are detected at the sampling time, depending on both the geometry and the time width of the input pulse. The transducers were placed 50 cm away from the sample (in the direction perpendicular to the largest faces of the samples). For measurements with $\vec{q}$ along x or y, the transducers were angled towards the sample at about 35° (depending on the sample's phase velocity), which gives an angle inside the sample of 45°, and a scattering angle that is twice this. The beam spread, as characterized by the angle $\Delta\theta$ from the beam axis at which the amplitude is reduced by 6 dB, is $\pm\Delta\theta \approx \pm 5°$, and is somewhat larger (about ±7°) inside the sample due to refraction. This results in a range of scattering angles from 75° to 104° (i.e., about ±14°). However, in this case, the geometry is not the limiting factor, because we were sampling at one particular arrival time. This limits the range of paths that can reach the detector at the sampling time to those whose travel time is equal to the time of the central path, plus or minus half of the time width of the input pulse. It is here that the long path lengths in the water tank help to reduce the spread in the scattered angle. The spread in the scattering angle, $\Delta\theta_s$, is reduced to about ±1.5° for an input pulse width of 20 μs. It must be noted that for all of these scattering angles, $\vec{q}$ has essentially the same direction, as it is only the finite size of the transducer and the finite thickness of the sample that have an effect on the direction of the scattering wave vector. In practice, the direction of $\vec{q}$ is limited by the accuracy with which the transducers were aligned, $\Delta\theta_{\vec{q}} = 1°$.

Once the field autocorrelation function has been measured, the appropriate $\vec{q}$ can be substituted into Eq. (9), and the mean square displacements can be found. The resulting expression is

$$\langle \Delta r_i^2(\tau)\rangle = -\frac{1}{2k^2 \sin^2\{\theta_s/2\}} \ln[g_1(\tau)], \tag{10}$$

where k is the magnitude of the wave vector in the scattering medium and i represents the appropriate Cartesian coordinate.

The near field configuration is much more compact, requiring only one plane wave input transducer and a small detector placed close to the sample. To avoid cancellation of the scattered waves, the detector must be small enough to detect a single speckle, which in the near field has a size comparable to the wavelength of the ultrasound.

The scattered field is sampled at one particular time, t_s, and therefore, by determining the set of single scattering paths of length t_s, the average scattering angle and scattering wave vector can be found. The details of this calculation are discussed in the Appendix, including the effects of the range of input angles from the transducer, the different scattering volumes, the angle dependent scattering amplitude, the angle

dependent wall transmission, and the small shear wave component in the walls. The basic result of this analysis is that we measure a mixture of the all of the components of the mean square displacement, with the magnitude of $\langle \vec{q} \rangle$ depending on the sampling time, such that

$$g_1(\tau) = \exp[-\bar{C}\langle \Delta r^2(\tau)\rangle'], \tag{11}$$

with

$$\langle \Delta r^2\rangle' = \langle \Delta r_x^2\rangle + \langle \Delta r_y^2\rangle + 2\tan^2\alpha\langle \Delta r_z^2\rangle \sim \langle \Delta r_x^2\rangle + \langle \Delta r_y^2\rangle. \tag{12}$$

Here the Cartesian directions are as defined in Fig. 3, α is an angle that depends on the scattering angle and is of order 20° in our experiments, and $\bar{C}$ is a constant that depends on t_s and on the magnitude of the wave vector in the sample. Thus, the near field method does not resolve the individual components of the mean square displacement of the scatterers, and therefore provides less information about the particle dynamics than the far field method. Its advantages are that the near field configuration can be used in small water tanks where there is not enough space to enable well collimated far-field beams to be used, and convenience in terms of experimental set up.

For both experimental configurations, once the field fluctuations are measured and the field autocorrelation function determined, the mean square displacements can be found using either Eqs. (10) or (11). As an example, we show results obtained on a fluidized suspension of 0.875-mm-diameter glass beads in a solution of glycerol in water. By varying the upward flow of the fluid, the dynamics of suspensions covering a wide range of particle concentrations was investigated (with particle volume fractions ϕ from 0.04 to 0.5), and by varying the concentration of glycerol in the suspending fluid, the particle Reynolds number that governs the flow regime could be set in the range of interest (from 0.007 to 7). Here we consider representative results for the case of a fluid mixture of 75% glycerol and 25% water, and particle Reynolds number 0.9. Figure 4 shows typical measurements of the mean square displacement of the glass beads as a function of time. At early times, $\langle \Delta r^2(\tau)\rangle \propto \tau^2$, meaning that the particles are moving ballistically with constant (although different) velocities. At later times $\langle \Delta r^2(\tau)\rangle$ rolls over to a weaker τ dependence as the particles begin to interact with their neighbors and their velocities change. This behavior can be modeled by using the phenomenological fitting function

$$\langle \Delta r^2(\tau)\rangle = \langle \Delta V^2\rangle\tau^2/[1 + (\tau/\tau_c)^{2-m}], \tag{13}$$

where $\langle \Delta V^2\rangle = V_{rms}^2$ is the particle velocity variance (which is equal to the mean square velocity, since $\langle V\rangle = 0$ for fluidized suspensions), τ_c is the average collision time, and m is an exponent that determines the long time power law dependence of $\langle \Delta r^2(\tau)\rangle$. From the collision time we can determine the dynamic correlation length ($d = \tau_c V_{rms}$), which is the average distance traveled by a particle before its velocity is significantly changed. Thus DSS gives important information on the temporal and spatial extent of correlations in the particles' motion, as well as measuring the magnitude of the rms particle velocity.

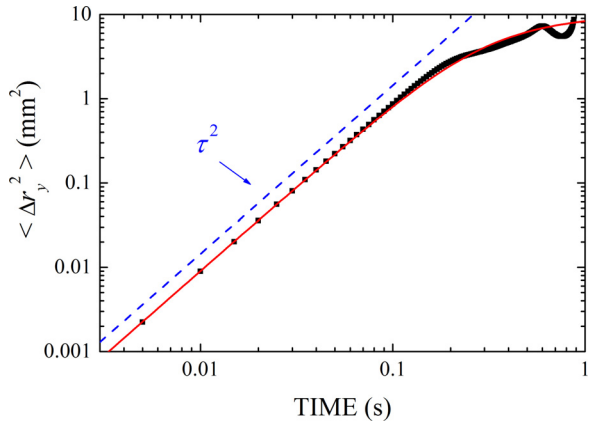

FIG. 4. (Color online) Mean square displacement of the particles in a fluidized suspension, along with a fit of the phenomenological function [Eq. (13)] that describes its time dependence (solid red curve). The dashed blue line indicates τ^2 behaviour, which is characteristic of the time-dependence for τ less than ~ 0.1 s.

IV. RESULTS AND DISCUSSION

Figure 5(a) shows an example of measurements of the three different components of V_{rms} in fluidized suspensions, as a function of the volume fraction of the solid particles.

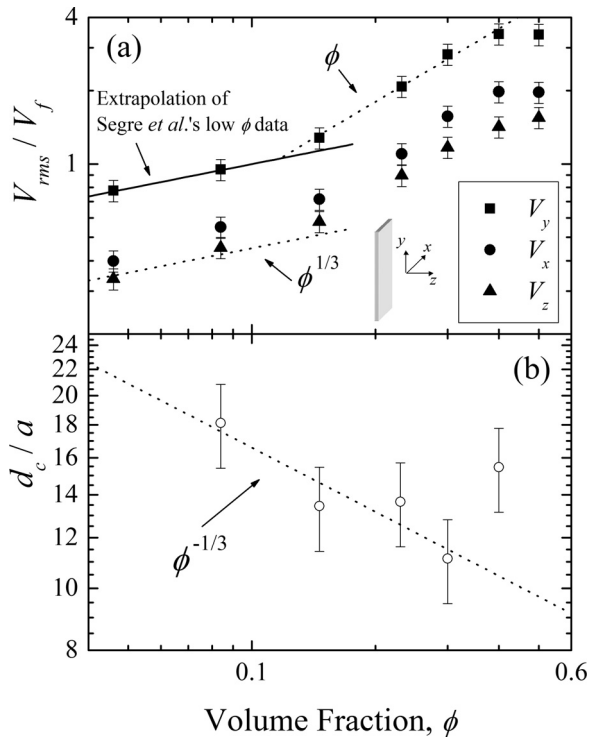

FIG. 5. (a) The three components of the root mean square velocity of the particles in a fluidized suspension measured using DSS (points), as well as an extrapolation of low volume fraction data measured using video imaging (Ref. 17) (solid line). The dashed lines are power law fits to the data. The rms velocities are normalized by the fluidization velocity V_f, the sample thickness $L_z = 36.5$ mm and the particle Reynolds number Re = 0.9. (b) The dynamic correlation length d_c measured by DSS for the same suspensions.

The data are normalized by the fluid flow velocity at each volume fraction, which is a relevant velocity scale in the suspension. In these samples, the component of the particle velocity along the direction of fluid flow (y) is larger than the two horizontal components, and the component along the thin dimension of the cell is less than that along the larger dimension. At low volume fractions, the data are in agreement with previous low volume fraction (<0.05) measurements of the y component, performed on very low Reynolds number sedimenting suspensions by direct video imaging.[17] The full three dimensional dynamic correlation length (d_c) is plotted in Fig. 5(b) for the same suspensions, showing the range of dynamic information that can be measured using DSS.

To test the reliability of the far-field DSS techniques, we measured the root mean square velocity for several different scattering angles, with the geometry arranged so that the direction of $\vec{q}$ remained the same. To arrange this condition, we placed two transducers on the same side of the sample, one inclined towards the sample at $-\theta_w$ and the other at $+\theta_w$. The $\vec{q}$ resulting from this setup points along the z-axis, and has a magnitude that depends on the scattering angle:

$$|\vec{q}| = 2k \sin\left[\frac{\theta_s}{2}\right], \tag{14}$$

$$\theta_s = 180^\circ - 2\sin^{-1}\left[\frac{v_p}{c_w}\sin\theta_w\right]. \tag{15}$$

The mean square displacements measured at three different scattering angles are compared in Fig. 6. They agree quite well over most of the time range, with only a slight difference in the $\theta_s = 110^\circ$ results as the time dependence of $\langle \Delta r_z^2(\tau)\rangle$ rolls-over from its initial τ^2 behavior. These measurements also check that the mean square displacement does not depend on the magnitude of q, at least over the limited range of values that we used (all of our data has $90^\circ < \theta_s < 180^\circ$). This means that any possible structure factor effects are not important on the length scales (q^{-1}) at which the measurements are performed. This is reasonable, because q^{-1} is less

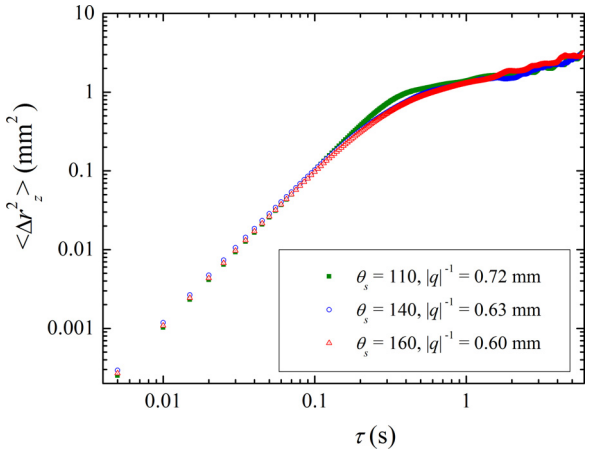

FIG. 6. (Color online) Test of the far field DSS technique. The measured mean square displacement of the scatterers along the z-direction is shown for three different scattering angles.

TABLE I. Comparison of the values of V_{rms} measured using the near and far-field DSS techniques.

	Near field	Far field		
	V'_{rms}	V_{rms}	$V'_{rms} = \sqrt{V_{rms,x}^2 + V_{rms,y}^2 + 2V_{rms,z}^2 \tan^2\alpha}$	% diff.
#1	1.74	1.86	1.81	+3.9
#2	2.18	2.12	2.06	−5.8

than a bead diameter, and therefore we are sensitive to the motion of individual beads.

The far-field DSS technique can give more information about the scatterers and the analysis is more straightforward. However, the near-field technique is more convenient and compact to set up, and thus it is important to compare the results of the two techniques to test their self-consistency. By using two methods and comparing the results, we are also testing the accuracy of both of the measurement techniques.

The results of two such tests are shown in Table I. In the first column, the near-field measurement of the approximate three-dimensional root mean square velocity is shown. The next column gives the full three-dimensional root mean square velocity, found by combining the far-field measurements of all three components. The last two columns show the expected near-field measurement values calculated from the far-field measurements [see the Appendix and Eq. (A12)], and the percent difference from what was actually measured (i.e., between columns one and two). The two techniques agree to within ±5%, which is also within the expected uncertainties in each (about 15% for the near-field calculation, and 10% for the far-field measurements). Therefore, the two techniques are consistent with each other, providing a check on the validity of the near-field technique and the accuracy of DSS in general.

V. CONCLUSIONS

In this paper, we describe the technique of DSS, an ultrasonic correlation spectroscopy technique that we have developed for investigating the dynamics of scattering particles in the weak scattering limit where the incident waves are scattered only once. Two different experimental approaches are explained, one using far-field generation and detection of the ultrasonic waves, and the other using near-field detection to take advantage of the relative ease with which subwavelength hydrophones can resolve a dynamic speckle pattern close to the sample surface. By using the information present in the temporal fluctuations of the singly scattered waves from the sample, we show how the root mean square displacement of the scatterers can be measured accurately as a function of evolution time. DSS is ideally suited to the measurement of the complex motion of scatterers at high volume fractions, opening a class of systems, whose properties may be inaccessible with dynamic optical techniques, to investigation using ultrasonic techniques.

ACKNOWLEDGMENTS

Support for this research from NSERC's Discovery Grant Program is gratefully acknowledged.

APPENDIX

In this appendix, we describe how DSS can be performed in the near field, giving a detailed explanation of the calculations required for our sample geometry. These calculations will also serve as a model for adapting the near-field method to other sample shapes and sizes, containing different types of scattering objects, where the numerical details will likely be different.

To relate the near field DSS sampling times to the scattering angle, and $\vec{q}$, we need to consider the ray diagram in Fig. 7, where many of symbols used in this appendix are defined. For a finite-size planar transducer, the input beam at the sample contains a range of angles, with different amplitudes. The rays then enter the wall, where rays incident at angle θ_{ow} are refracted into a different direction, θ_{op}. There is also coupling into a small amplitude shear wave, but the range of input angles from the transducer is small enough that this is negligible. As the rays enter the sample, they are refracted into an angle θ_o. At a depth s, the ultrasound is scattered towards the hydrophone, and on its way the ultrasound passes through the exit wall as either a shear or longitudinal wave. The time taken to travel this path, as compared to the time taken for a pulse to travel ballistically straight through the sample to the hydrophone, is given by

$$t_s = \frac{L_{TtoS}}{c_w}\left[\frac{1}{\cos\theta_{ow}} - 1\right] + \frac{L_{wall}}{c_{wall}}\left[\frac{1}{\cos\theta_{op}} - 2\right] + \frac{L_{wall}}{c_{wall2}\cos\theta_{p2}} + \frac{s}{v_g\cos\theta_o} + \frac{L-s}{v_g\cos\{\theta_s-\theta_o\}} - \frac{L}{v_g} + \frac{d}{c_w}\left[\frac{1}{\cos\theta_w} - 1\right], \tag{A1}$$

where the phase velocity in the exit wall (c_{wall2}) can be that of either the longitudinal or shear modes. Here all angles and distances are defined in Fig. 7, c_w and c_{wall} are the phase velocities in water and the entrance wall, respectively, and v_g is the group velocity in the fluidized suspension. We can also write two equations for the scattering radius (the perpendicular distance to the scattering point from the ballistic path through the sample),

$$r(s) = L_{TtoS}\tan\theta_{ow} + L_{wall}\tan\theta_{op} + s\tan\theta_o \tag{A2}$$

and

$$r(s) = \{L-s\}\tan\{\theta_s-\theta_o\} + L_{wall}\tan\theta_{p2} + d\tan\theta_w. \tag{A3}$$

For a particular scattering depth (s), sampling time, and wall mode, Eqs. (A1)–(A3) can be numerically inverted to find the scattering angle (θ_s), the input angle (θ_{ow}), and the scattering radius. At a given time, this gives a range of possible scattering and input angles (corresponding to the range of scattering depths from $s=0$ to $s=L$) for each wall mode. For the longitudinal case (where the scattered waves pass through the exit wall as longitudinal waves), the range of possible angles is quite small, so we use the mean value of the angles in the correlation function. However, for the shear case, the range of angles is larger, so we must account for this effect and average the correlation function over the scattering depth (s). Since the field detected by the hydrophone is a superposition of uncorrelated waves that have gone through the exit wall as either a shear or longitudinal mode, the field correlation function, for a particular sampling time t_s, can be decomposed into a shear and a longitudinal part,

$$\begin{aligned} g_1(\tau) &= \frac{\langle\{\psi_L(t)+\psi_T(t)\}\{\psi_L^*(t+\tau)+\psi_T^*(t+\tau)\}\rangle}{\langle\{\psi_L(t)+\psi_T(t)\}\{\psi_L^*(t)+\psi_T^*(t)\}\rangle} \\ &= \frac{\langle\psi_L(t)\psi_L^*(t+\tau)\rangle + \langle\psi_T(t)\psi_T^*(t+\tau)\rangle}{\langle\psi_L(t)\psi_L^*(t)\rangle + \langle\psi_T(t)\psi_T(t)\rangle} \\ &\equiv \frac{g'_L(\tau)+g'_T(\tau)}{g'_L(0)+g'_T(0)}, \end{aligned} \tag{A4}$$

where

$$g'_L(\tau) = \frac{\int A_L(t')\langle e^{i\Delta\phi_L(\tau,t')}\rangle u^2(t'-t_s)dt'}{\int u^2(t'-t_s)dt'}, \tag{A5}$$

and

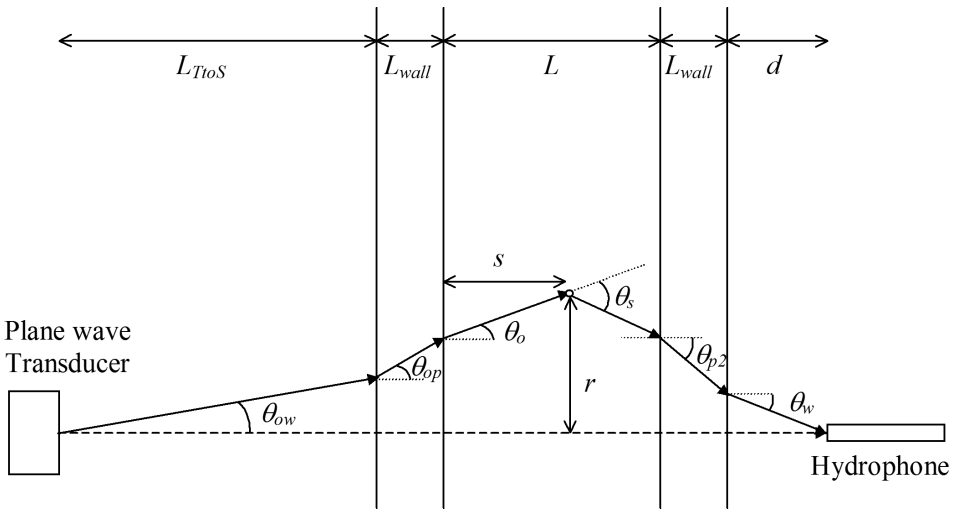

FIG. 7. Scattering geometry for near field DSS, used in the timing calculations.

$$g'_T(\tau) = \frac{\int\int u^2(t'-t_s)A_T(s,t')\langle e^{i\Delta\phi_T(\tau,s,t')}\rangle dt'ds}{\int\int u^2(t'-t_s)dt'ds}. \quad \text{(A6)}$$

Here, $A_L(t')$ and $A_T(s,t')$ give the relative intensities of the longitudinal and shear components, respectively (the details of which will be discussed below), $\Delta\phi_L(\tau,t') = \vec{q}_L(t')\cdot\Delta\vec{r}(\tau)$ and $\Delta\phi_T(\tau,s,t') = \vec{q}_T(s,t')\cdot\Delta\vec{r}(\tau)$ are the phase changes due to the motion of the particles, and $u(t')$ is the input pulse envelope.

The next step is to approximate the averages $\langle e^{i\Delta\phi_L(\tau,t')}\rangle$ and $\langle e^{i\Delta\phi_T(\tau,s,t')}\rangle$ so that the integrals in Eqs. (A5) and (A6) can be evaluated. Figure 8 shows the scattering vector $\vec{q}$, which is inclined above the x-y plane by an angle $\alpha = \theta_o - \theta_s/2$. There is cylindrical symmetry about the z-axis, so the set of possible $\vec{q}$ forms a cone. This gives

$$\begin{aligned} q_x &= q\cos\alpha\cos\beta, \\ q_y &= q\cos\alpha\sin\beta, \\ q_z &= q\sin\alpha, \end{aligned} \quad \text{(A7)}$$

where β is the angle of rotation about the z-axis. The phase average can be expanded to give

$$\begin{aligned} \langle e^{-i\Delta\phi}\rangle &\approx 1 - \frac{1}{2}\langle\Delta\phi^2\rangle \\ &= 1 - \frac{1}{2}\langle\{q_x\Delta r_x + q_y\Delta r_y + q_z\Delta r_z\}^2\rangle. \end{aligned} \quad \text{(A8)}$$

Substituting Eq. (A7) into Eq. (A8), averaging over β, and using

$$\begin{aligned} &\langle\cos^2\beta\rangle = \langle\sin^2\beta\rangle = \frac{1}{2}, \\ &\langle\cos\beta\rangle = \langle\sin\beta\rangle = \langle\cos\beta\sin\beta\rangle = 0, \\ &q^2 = 4k^2\sin^2\left[\frac{\theta_s}{2}\right], \end{aligned} \quad \text{(A9)}$$

gives

$$\begin{aligned} \langle e^{-i\Delta\phi}\rangle \sim 1 - 2k^2\sin^2\left[\frac{\theta_s}{2}\right]\Bigg\{\left[\frac{1}{2}\langle\Delta r_x^2\rangle + \frac{1}{2}\langle\Delta r_y^2\rangle\right] \\ \times\cos^2\alpha + \langle\Delta r_z^2\rangle\sin^2\alpha\Bigg\}. \end{aligned} \quad \text{(A10)}$$

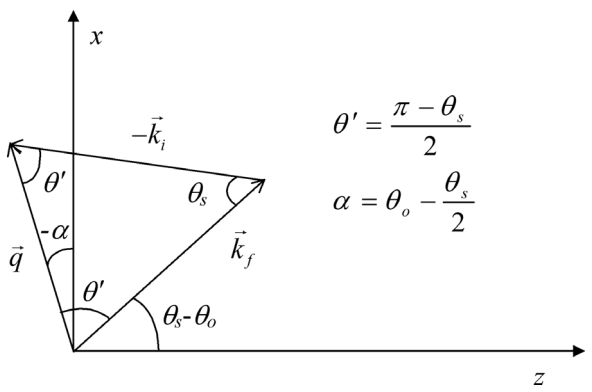

FIG. 8. Scattering wave vector diagram for near field DSS.

For our sample geometry and the longitudinal case, α is about $-17°$, giving $\cos^2\alpha = 0.92$ and $\sin^2\alpha = 0.08$, which means that the contribution of the z-component to Eq. (A10) is very small. For the shear case, however, α is about $-30°$, giving $\cos^2\alpha = 0.75$ and $\sin^2\alpha = 0.25$; even in this case, given that $\langle\Delta r_z^2\rangle$ is already small, and that the shear component is smaller than the longitudinal one, this means that the z-component contributes very little to the phase change in this case too. Therefore,

$$\langle e^{-i\Delta\phi}\rangle \approx 1 - k^2\sin^2\left[\frac{\theta_s}{2}\right]\cos^2\alpha\langle\Delta r^2\rangle', \quad \text{(A11)}$$

where the measured mean square displacement $\langle\Delta r^2\rangle'$ is approximately equal to the full three-dimensional mean square displacement $\langle\Delta r^2\rangle$ (because the z-component of the mean square displacement tends to be small in our experiments). Thus,

$$\begin{aligned} \langle\Delta r^2\rangle' &= \langle\Delta r_x^2\rangle + \langle\Delta r_y^2\rangle + 2\tan^2\alpha\langle\Delta r_z^2\rangle \\ &\approx \langle\Delta r_x^2\rangle + \langle\Delta r_y^2\rangle \\ &\approx \langle\Delta r^2\rangle. \end{aligned} \quad \text{(A12)}$$

The longitudinal component of the field autocorrelation function can be simplified to

$$\begin{aligned} g_L(\tau) \approx \frac{\int u^2(t'-t_s)A_L dt'}{\int u^2(t'-t_s)dt'}\Bigg[1 - k^2\langle\Delta r^2(\tau)\rangle \\ \times\frac{\int u^2 A_L\sin^2\left\{\frac{\theta_s(t')}{2}\right\}\cos^2\alpha dt'}{\int u^2 A_L dt'}\Bigg], \end{aligned}$$

which can be re-written as

$$g_L(\tau) \equiv \bar{A}_L[1 - \bar{C}_L\langle\Delta r^2(\tau)\rangle]. \quad \text{(A13)}$$

Here, the definitions of the two average quantities $\bar{A}_L$ and $\bar{C}_L\langle\Delta r^2(\tau)\rangle$ can be easily seen by comparing the above two equations.

The shear component can similarly be simplified to

$$\begin{aligned} g_T(\tau) \approx \frac{\int u^2(t'-t_s)\left[\int A_T ds\right]dt'}{\int u^2(t'-t_s)dt'}\Bigg[1 - k^2\langle\Delta r^2(\tau)\rangle \\ \times\frac{\int u^2\left[\int ds A_T\sin^2\left\{\frac{\theta_s}{2}\right\}\cos^2\alpha\right]dt'}{\int u^2\left[\int A_T ds\right]dt'}\Bigg] \text{ and} \end{aligned}$$

$$g_T(\tau) \equiv \bar{A}_T\left\{1 - \bar{C}_T\langle\Delta r^2(\tau)\rangle\right\}. \quad \text{(A14)}$$

From Eq. (A4), this gives an overall field correlation function of

$$g_1(\tau) = 1 - \frac{\bar{C}_L + \frac{\bar{A}_T}{\bar{A}_L}\bar{C}_T}{1 + \frac{\bar{A}_T}{\bar{A}_L}} \langle \Delta r^2(\tau) \rangle$$
$$\equiv 1 - \bar{C}\langle \Delta r^2(\tau) \rangle \sim \exp\left[-\bar{C}\langle \Delta r^2(\tau) \rangle\right]. \quad \text{(A15)}$$

The factor $\bar{C}$ can be found by numerically evaluating the integrals in Eqs. (A13) and (A14), given the weighting factors and angles that appear in these equations.

The angular dependence of the longitudinal weighting factor is given by

$$A_L = \int_{s=0}^{L} [A_{in} A_{sc} T_l]^2 r \cos\theta_w \frac{dr}{dt_s} ds$$
$$\approx L[A_{in} A_{sc} T_l]^2 r \cos\theta_w \left\{\frac{dr}{dt_s}\right\}, \quad \text{(A16)}$$

where A_{in} is the amplitude of the input wave at the angle θ_{ow}, A_{sc} is the scattering amplitude from a single particle (see next paragraph) at the scattering angle θ_s, T_l is the output wall transmission coefficient for a longitudinal wave at the angle θ_{p2}, the factor of rdr/dt_s represents the scattering volume, and $\cos\theta_w$ describes the angular response of the detector. Similarly, the shear weighting factor can be written

$$A_T \approx [A_{in} A_{sc} T_T]^2 r \cos\theta_w \frac{dr}{dt_s}. \quad \text{(A17)}$$

To evaluate Eqs. (A16) and (A17), the scattering amplitude A_{sc} was calculated as a function of angle using an effective medium theory. In this theory, each scattering unit is modeled as a coated glass sphere, embedded in an effective medium that represents the effect of the rest of the scatterers.[23,24] This model has been shown to give a remarkably accurate description of wave propagation in particulate suspensions,[23] so that it is not necessary to measure A_{sc} experimentally to determine A_L and A_T. Given the material parameters, the wall transmission coefficients can be calculated using standard acoustic mismatch theory. By expressing all of the angle and amplitude factors as a function of the sampling time and s, $\bar{C}_L$, $\bar{C}_T$, $\bar{A}_L$, and $\bar{A}_T$ can all be calculated, as shown in Fig. 9. Then, given the longitudinal and shear results, $\bar{C}$, as defined in Eq. (A15), can be evaluated for the sample thicknesses used in the experiments, enabling the particle dynamics to be determined from the correlation function, Eq. (11), for near-field DSS.

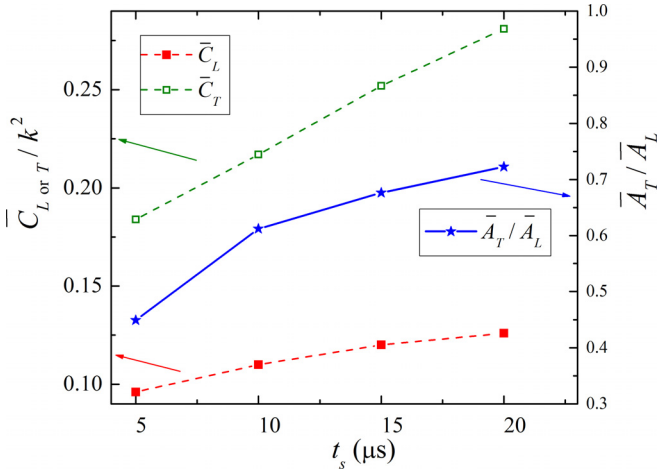

FIG. 9. (Color online) Comparison of the contributions to the near-field DSS correlation function of scattered waves that pass through the exit wall of the sample as either shear or longitudinal modes.

[1]D. H. Evans and W. N. McDicken, *Doppler Ultrasound: Physics, Instrumentation, and Clinical Applications*, 2nd ed. (Wiley, New York, 2000), pp. 1–427.
[2]M. L. Cowan, J. H. Page, and D. A. Weitz, "Velocity fluctuations in fluidized suspensions probed by ultrasonic correlation spectroscopy," Phys. Rev. Lett. **85**, 453–456 (2000).
[3]M. L. Cowan, I. P. Jones, J. H. Page, and D. A. Weitz, "Diffusing acoustic wave spectroscopy," Phys. Rev. E **65**, 066605 (2002).
[4]M. L. Cowan, "Strong scattering of ultrasonic waves in fluidized suspensions: Wave propagation, spectroscopy techniques and particle dynamics," Ph.D. thesis, University of Manitoba, Winnipeg, Manitoba, Canada (2001).
[5]A. Aubry and A. Derode, "Random matrix theory applied to acoustic backscattering and imaging in complex media," Phys. Rev. Lett. **102**, 084301 (2009).
[6]J. Park, J. B. Kang, J. H. Chang, and Y. Yangmo, "Speckle reduction techniques in medical ultrasound imaging," Biomed. Eng. Lett., **4**, 32–40 (2014).
[7]It is also worth noting that speckles in weak scattering situations can sometimes be very useful, as in medical echography, for example, the specific properties of speckle for different tissues can make tissue differentiation possible, e.g., see M. L. Oelze, J. P. Kemmerer, G. Ghoshal, and R. M. Vlad, "Therapy monitoring and assessment using quantitative ultrasound," in *Quantitative Ultrasound in Soft Tissues*, edited by J. Mamou and M. L. Oelze (Springer, Dordrecht, 2013), Chap. 9, pp. 193–216.
[8]K. Igarashi, T. Norisuye, K. Kobayashi, K. Sugita, H. Nakanishi, and Q. Tran-Cong-Miyata, "Dynamics of submicron microsphere suspensions observed by dynamic ultrasound scattering techniques in the frequency-domain," J. Appl. Phys. **115**, 203506 (2014).
[9]K. Ishii, T. Iwai, and H. Xia, "Hydrodynamic measurement of Brownian particles at a liquid-solid interface by low-coherence dynamic light scattering," Opt. Express **18**, 7390–7396 (2010).
[10]K. Ishii, R. Yoshida, and T. Iwai, "Single-scattering spectroscopy for extremely dense colloidal suspensions by use of a low-coherence interferometer," Opt. Lett. **30**, 555–557 (2005).
[11]M. Kohyama, T. Norisuye, and Q. Tran-Cong-Miyata, "High frequency dynamic ultrasound scattering from microsphere suspensions," Polym. J. **40**, 398–399 (2008).
[12]M. Kohyama, T. Norisuye, and Q. Tran-Cong-Miyata, "Dynamics of microsphere suspensions probed by high frequency dynamic ultrasound scattering," Macromolecules **42**, 752–759 (2009).
[13]M. L. Cowan, D. Anache-Menier, W. K. Hildebrand, J. H. Page, and B. A. van Tiggelen, "Mesoscopic phase statistics of diffuse ultrasound in dynamic matter," Phys. Rev. Lett. **99**, 094301 (2007).
[14]A. Nagao, M. Kohyama, T. Norisuye, and Q. Tran-Cong-Miyata, "Simultaneous observation and analysis of sedimentation and floating motions of microspheres investigated by phase mode-dynamic ultrasound scattering," J. Appl. Phys. **105**, 023526 (2009).
[15]É. Guazzelli, "Sedimentation of small particles: How can such a simple problem be so difficult?," C. R. Mecanique **334**, 539–544 (2006).
[16]É. Guazzelli and J. Hinch, "Fluctuations and instability in sedimentation," Ann. Rev. Fluid Mech. **43**, 97–116 (2011).
[17]P. N. Segrè, E. Herbolzheimer, and P. M. Chaikin, "Long-range correlations in sedimentation," Phys. Rev. Lett. **79**, 2574–2577 (1997).
[18]A. Nagao, T. Norisuye, M. Kohyama, T. Yawada, and Q. Tran-Cong-Miyata, "Collective motion of microspheres in suspensions observed by phase-mode dynamic ultrasound scattering technique," Ultrasonics **52**, 628–635 (2012).
[19]X. Lei, B. J. Ackerson, and P. Tong, "Settling statistics of hard sphere particles," Phys. Rev. Lett. **86**, 3300–3303 (2001).
[20]B. J. Berne and R. Pecora, *Dynamic Light Scattering with Applications to Chemistry, Biology and Physics* (Dover Publications, Mineola, NY, 2000), pp. 1–384.

[21]P. Tong, I. Goldburg, C. K. Chan, and A. Sirivat, "Turbulent transition by photon-correlation spectroscopy," Phys. Rev. A **37**, 2125–2133 (1988).
[22]W. H. Press, S. A. Teukolsky, W. T. Vetterling, and B. P. Flannery, *Numerical Recipes in C* (Cambridge University Press, Cambridge, 1992), Chap. 13, pp. 537–608.
[23]M. L. Cowan, K. Beaty, J. H. Page, Z. Liu, and P. Sheng, "Group velocity of acoustic waves in strongly scattering media: Dependence on the volume fraction of scatterers," Phys. Rev. E **58**, 6626–6636 (1998).
[24]X. Jing, P. Sheng, and M. Zhou, "Acoustic and electromagnetic quasimodes in dispersed random media," Phys. Rev. A **46**, 6513–6538 (1992).